RESEARCH ARTICLE

submitted to Quartely Journal of the Royal Meteorological Society

The relationship between precipitation and its spatial organisation in the trades observed during EUREC^{4}A

Jule Radtke[1, 2] | Ann Kristin Naumann[3, 1] | Martin Hagen[4] | Felix Ament[1, 3]

[1]Meteorological Institute, Center for Earth System Research and Sustainability, Universität Hamburg, Hamburg, Germany

[2]International Max Planck Research School on Earth System Modelling, Max Planck Institute for Meteorology, Hamburg, Germany

[3]Max Planck Institute for Meteorology, Hamburg, Germany

[4]Deutsches Zentrum für Luft- und Raumfahrt, Institut für Physik der Atmosphäre, Oberpfaffenhofen, Germany

Correspondence
Jule Radtke, Meteorological Institute, Universität Hamburg, Hamburg, 20146, Germany
Email: jule.radtke@uni-hamburg.de

Funding information
Deutsche Forschungsgemeinschaft (DFG, German Research Foundation) under Germany's Excellence Strategy – EXC 2037 'CLICCS - Climate, Climatic Change, and Society' – Project Number: 390683824

Trade wind convection organises into a rich spectrum of spatial patterns, often in conjunction with precipitation development. This raises the question of the role of spatial organisation for precipitation and vice versa. We analyse scenes of trade wind convection scanned by the C-band radar Poldirad during the EUREC^{4}A field campaign to investigate how trade wind precipitation fields are spatially organised, quantified by the cells' number, mean size and spatial arrangement, and how this matters for precipitation characteristics. During EUREC^{4}A, a mean rain cell size of about 5 km and mean distance to the nearest neighbouring cell of about 14 km were most common. We find that the amount of precipitation in a scene is influenced in a different way than the intensity of precipitation by the spatial organization. While precipitation amount increases with mean cell size and number, as it scales well with precipitation fraction, precipitation intensity increases predominantly with mean cell size. The increase of precipitation intensity with mean cell size, however, differs with the moisture regime. It is stronger in dry than in moist scenes. Dry scenes typically contain fewer cells with a higher degree of clustering than moist scenes. The highest precipitation intensities hence typically occur in scenes with on average large and few cells and a high degree of clustering, while the highest precipitation amounts typically occur in scenes with on average large and numerous cells and a low degree of clustering. Our analyses suggest that the cells' spatial arrangement is important for precipitation formation in dry environments, but mainly weakly correlated with precipitation characteristics and thus of second order importance across all regimes. Our analyses highlight the importance of cell size, as it influences both the intensity and amount of precipitation.

KEYWORDS
precipitating shallow convection, spatial organization, field campaign, observations, trade wind regime

1 | INTRODUCTION

The trades are raining. In early reviews of trade wind convection, this fact is given minimal attention (e.g. Betts, 1997; Siebesma, 1998; Stevens, 2005). In these reviews, trade wind convection is mainly described as non-precipitating and randomly distributed popcorn convection. Since the trade-wind region and its clouds, important to cool our earth, emerged as central to the issue of climate change because they dominate the spread in climate sensitivity (e.g. Bony and Dufresne, 2005; Vial et al., 2013), new studies have proven this description to be wrong. Field studies and satellite imagery in particular have emphasized how trade-wind convection organises into a rich spectrum of spatial patterns, often in conjunction with precipitation development (Snodgrass et al., 2009; Stevens et al., 2020; Schulz et al., 2021). This raises the question of the role of spatial organisation for precipitation and vice versa, which is not yet well understood. To address this question, this study uses observations from the recent field campaign EUREC^{4}A (ElUcidating the RolE of Cloud-Circulation Coupling in ClimAte, Stevens et al., 2021) and investigates the spatial behaviour of precipitating convection and how it matters for precipitation characteristics in the trades.

A preceding field campaign, RICO (Rain In Cumulus over the Ocean, Rauber et al., 2007), showed that shallow precipitation is common with about one-tenth of the cloudy areas raining (Nuijens et al., 2017; Snodgrass et al., 2009). Other studies estimate that warm rain showers contribute 20-30% to the total precipitation amount and 70% to the total precipitation area over tropical oceans (Lau and Wu, 2003; Short and Nakamura, 2000). Precipitation might be a key to understand the vertical thermodynamic structure, cloudiness, and spatial organisation of the trade regime (e.g. Vogel et al., 2016). However, controls on precipitation in shallow convection are still poorly constrained and the representation of precipitation in large eddy simulations that explicitly account for rain-formation processes differs largely (vanZanten et al., 2011). An understanding how spatial organisation influences precipitation rates, might help interpret and reduce these differences (Stevens et al., 2021).

Besides quantifying precipitation rates in the trades, the RICO campaign also brought attention to the spatial organisation of convection in the trades and highlighted that precipitation was often observed with arc-shaped cloud patterns associated with cold pool outflows (Snodgrass et al., 2009; Zuidema et al., 2012). These cold pool signatures reflect how precipitation links processes acting on different scales. The evaporation of precipitation on the micro scale can induce cold pools (Seifert and Heus, 2013; Touzé-Peiffer et al., 2021) and local circulations on the mesoscale, which trigger the birth of new convective cells. These local circulations may change the characteristics of clouds and therefore also precipitation formation. Precipitation, convection, and their spatial patterns or organisation are thus highly intertwined. However, while recent studies have focused on cloud patterns (e.g. Rasp et al., 2019; Denby, 2020; Bony et al., 2020), an investigation of precipitation patterns in the trades and the role of spatial organisation for precipitation and vice versa from the viewpoint of precipitation is lacking. Bony et al. (2020) show that cloud patterns differ in their cloudiness and net radiative effect. How do precipitations characteristics relate to precipitation patterns?

To address our question, we investigate scenes of trade wind convection scanned by the C-band radar Poldirad (Polarization Diversity Radar, Hagen et al., 2021) during the EUREC^{4}A field campaign, which took place in January and February 2020 in the western tropical North Atlantic near Barbados. We analyse how trade wind precipitation fields are spatially organised in these scenes and how this relates to the scenes' precipitation amount and intensity. While the amount of precipitation is related to the scene heating and drying (e.g Nuijens et al., 2009), the intensity of precipitation is important e.g. in a local sense for the triggering of cold pools (Snodgrass et al., 2009). Organization is not straight forward to define, and different metrics weight different attributes of organisation more or less strongly. We

choose to jointly analyse three characteristics of spatial organisation: the number, size, and spatial arrangement of cells. Given the relationship between water vapour, precipitation and organisation found in earlier studies (e.g Nuijens et al., 2009; Bretherton and Blossey, 2017), we further include vertically integrated water vapour as a supplementary explanatory variable in our analysis.

The data and methods used in this study are described in §2. First, we investigate the spatial organisation in trade wind precipitation fields (§3) by analysing the number, size, and spatial arrangement of rain cells and how they covary (§3.1). We show how the moisture environment of rain cells relates to their spatial behaviour and identify two moisture regimes (§3.2). With this information, we will analyse and interpret the relationship between the cells' spatial organisation and the amount and intensity of precipitation in §4. Finally, we show how the relations between organisation and precipitation behave in the diurnal cycle (§5), before we conclude in §6.

2 | DATA AND METHODOLOGY

2.1 | EUREC^{4}A field campaign

EUREC^{4}A was designed to elucidate the coupling between clouds, circulation, and convection (Bony et al., 2017). The field campaign took place in January and February 2020 in the western tropical Atlantic, with most operations based out of the island Barbados and targeting a comprehensive observation of clouds, precipitation, and their atmospheric and oceanic environment in the trades upwind of Barbados. A thorough overview of EUREC^{4}A is provided in Stevens et al. (2021). Here, we exploit observational data from the C-band radar Poldirad (Hagen et al., 2021) that scanned fields of precipitating trade wind convection upwind of Barbados. Furthermore, we include observations of vertically integrated water vapour from GNSS receivers (Bock et al., 2021) at the Barbados Cloud Observatory (Stevens et al., 2016).

2.1.1 | C-band research radar Poldirad

Poldirad is a polarimetric C-band research radar of the German Aerospace Center (DLR) (Schroth et al., 1988). During EUREC^{4}A, Poldirad was deployed on Barbados to provide a detailed view of the upstream precipitating trade wind convection and started to operate in February 2020. Poldirad took long-range surveillance scans at a 5 minute schedule with a maximum range of 375 km in a sector of about 100 degree eastward and upwind of Barbados, thus mapping out the spatial distribution of rain cells in the trade wind region. Here, we use the 2-dimensional gridded dataset interpolated on a 1 by 1 km grid with a size of 400 x 400 km^2 generated from these long surveillance scans. This dataset and Poldirads deployment in the EUREC^{4}A field campaign are described in Hagen et al. (2021).

For our analyses we examine the scans between 25 km and 175 km range as the radar beam remains below about 3 kilometres height up to this range and the frequency of strong echoes is approximately constant and to limit effects of sea clutter (see Hagen et al., 2021). The dataset by Hagen et al. (2021) provides a rain rate derived from the commonly used Z-R relationship $Z = 200R^{1.6}$ (Marshall et al., 1955). Here, we choose to use another Z-R relationship $Z = 148R^{1.55}$ as in Nuijens et al. (2009), which is explicitly attributed to shallow precipitation. Differences in the Z-R relationship lead to uncertainties in the absolute estimation of rain rates, which is, however, not the subject of this study. Please also note that peaks in rainfall are smoothed by the radar beam and the gridding, resulting in lower absolute rain rates. For each scene scanned by the radar, we calculate the precipitation amount P (rain rate averaged

across the entire scene, that is non-precipitating and precipitating area) and precipitation intensity I (rain rate averaged across the precipitating area only), whereby $P = I \cdot F$ with F the rain fraction. To give an overview of the dataset, Fig. 1 shows the time series of both P and I. Gaps in a continuous operation are caused by failures and limited personal resources. In our subsequent analyses we exclude radar scans from the period 13-15 February because of high clouds (Villiger et al., 2021). We also exclude all scans with less than five precipitating cells as a characterization of the spatial arrangement is difficult for scenes with few objects. The dataset captures a variability in P up to roughly 0.2 mm h^{-1}, which compares well to precipitation amounts observed in the RICO campaign (Nuijens et al., 2009), and I up to roughly 4 mm h^{-1}.

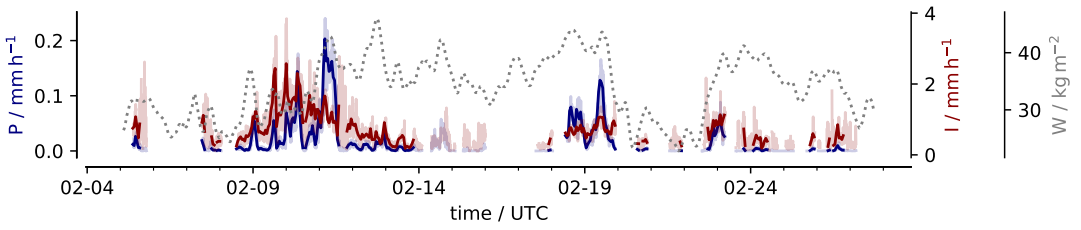

FIGURE 1 Time series of precipitation amount P, precipitation intensity I (thick lines display hourly means of the dataset used in the analysis, shading full dataset), and integrated water vapour W.

2.1.2 | Integrated Water Vapour Observations

To analyse the moisture environment of the rain cells, we use integrated water vapour W observations from GNSS receivers (Bock et al., 2021) installed at the Barbados Cloud Observatory. This dataset provides high temporal resolution integrated water vapour measurements at a 5 minute time interval. To provide an estimate of W for the scenes scanned by the radar to the east, we shift the time series of W by 100 km (that is, to the scene center approximately) assuming a mean wind speed of 6 m s^{-1} and smooth the time series with a running mean of 100 km / 6 m s^{-1} to account for a field mean. The integrated water vapour field is rather smooth so that changes in the interpolation details do not lead to substantial differences. The time series of W is shown as well in Fig.1.

2.2 | Identification of rain cells and derivation of their spatial attributes

To identify the rain cells that populate each scene we follow Brueck et al. (2020). We use a lower threshold of 0.1 mm h^{-1}, that is ~ 7 dBZ, to define a rain mask that segments precipitating objects from their non-precipitating environment. The rain cells are derived by a 2D watershed segmentation technique based on the local precipitation maxima. To find the local maxima the precipitation field is smoothed with a Gaussian filter. The filtering is not applied to, and does not affect the precipitating area and rate. The local maxima serve as starting points for the watershed procedure. In this procedure, the precipitating neighbourhood surrounding a local maximum is filled until it gets into contact with another neighbourhood. Due to possible regridding artefacts we only consider rain cells of minimum two pixel size. Furthermore, we exclude rain cells that touch the scene boundary. Figure 2 shows the segmentation for one exemplary scene.

After the segmentation procedure, we calculate for each scene the cells' geometrical properties size, number and dis-

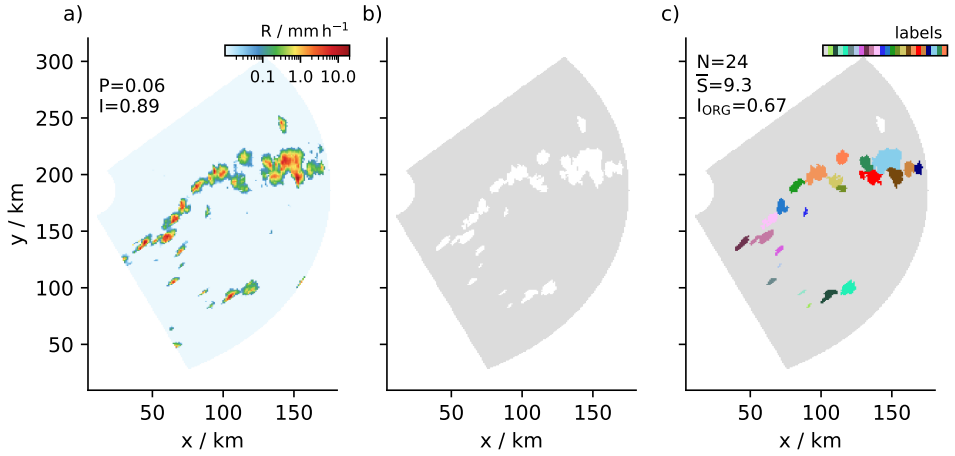

FIGURE 2 Example scene of a) rain rate, b) rain mask, and c) rain cell segmentation from 2020-02-11 00:50. For symbols see text.

tances between cells, from which we derive the attributes of spatial organisation that we will use in our analyses. Size, number, and distances are common ingredients in metrics of organisation, e.g. in the Simple Convection Aggregation Index SCAI (Tobin et al., 2012), the Convective Organisation Potential COP (White et al., 2018), or the Radar Organisation Metric ROME (Retsch et al., 2020). However, these metrics all include and weight these spatial properties in their own manner. We want to investigate the individual controls and choose to analyse the three individual basic properties jointly, instead of focusing on one organisation metric that mixes spatial properties.

For each scene, we derive the mean cell size $\overline{S}$, which we express in terms of the area equivalent diameter to provide a length scale similar to the distances between the cells. We will provide an overview of the individual cell sizes and show how the mean cell size scales with the distribution of cell sizes in a scene in §3. The product of $\pi/4 \cdot \overline{S}^2$ and the number of cells N equals the precipitating area $F_A = F \cdot A_{\text{scene}}$ with A_{scene} the scene area. The first two measures, $\overline{S}$ and N, hence, inform about the spatial composition of the precipitation area. We will use this relation in our analyses. The time series of $\overline{S}$ and N are shown in Fig. 3a,b.

To assess the spatial arrangement of cells, we use the index I_{ORG} (Weger et al., 1992; Tompkins and Semie, 2017). Please note that the naming of I_{ORG} might be misleading here, as we consider spatial arrangement as only one attribute of spatial organisation. The I_{ORG} is a metric of spatial arrangement based on nearest-neighbour distances and compares the observed distances between the cells to the distances of a random distribution. If nearest-neighbour distances are on average smaller than expected from a random distribution, the cells are considered clustered, otherwise regularly distributed. The time series of I_{ORG} is shown in Fig. 3c. Formally, I_{ORG} is defined as the integral below the curve of the cumulative density function of the actual observed nearest-neighbour distances (NNCDF) plotted against the NNCDF for a random distribution of the cells. A value of 0.5 corresponds to a random distribution, values larger than 0.5 indicate clustering, whereas values smaller than 0.5 indicate regularly distributed cells. To obtain the random distribution of distances for our domain size, we follow Brueck et al. (2020) and randomly distribute disks with the same areas and same number as the cells present in the scene domain. The random distribution results by

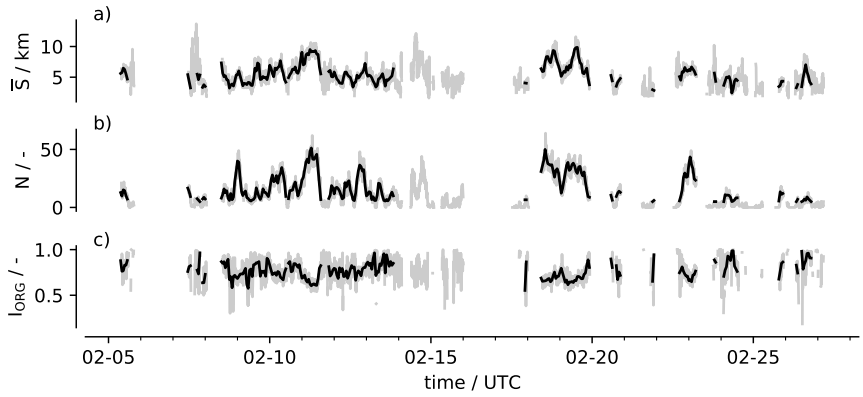

FIGURE 3 Time series of a) mean cell size $\overline{S}$, b) number of cells N and c) the spatial arrangement of cells quantified by the I_{ORG} (thick lines display hourly means of the dataset used in the analysis, shading full dataset).

taking the mean over hundred realizations of this procedure. As a consistency check, we also investigated a second metric of spatial arrangement based on the distances between all possible pairs of cells (Tobin et al., 2012), which compares the observed mean all-neighbour distance to the random mean all-neighbour distance. Both metrics show the same relationships, so that we only show the I_{ORG} in the remainder of this manuscript.

The time series in Fig. 3 indicate that $\overline{S}$, N, and I_{ORG} do not vary independently from each other. $\overline{S}$ and N often tend to increase and decrease similarly and decreases in I_{ORG} tend to go along with increases in N, e.g. on 11 or 19 february. Figure 4 provides an overview of the correlations between $\overline{S}$, N, I_{ORG}, P and I across the whole dataset. As indicated by the time series, $\overline{S}$ and N are positively correlated. The I_{ORG} and N are negatively correlated and I_{ORG} and $\overline{S}$ are weakly negatively correlated. In the following, we will work our way from top to bottom in Fig. 4. We will first look more closely at $\overline{S}$, N, and I_{ORG} and investigate and interpret how and why they covary (§3). To do so, we will span a phase space of $\overline{S}$ and N, as in Brueck et al. (2020). We will use this phase space in our subsequent analyses to interpret the correlations shown in Fig. 4 in more detail. Analysing organisation and precipitation in the phase space will help us to identify two moisture regimes (§3.2), show that competing effects lead to the weak correlation of P and I with I_{ORG} (§4) and that I predominantly increases with $\overline{S}$, but that this increase differs with the moisture regime.

3 | HOW ARE TRADE WIND PRECIPITATION FIELDS SPATIALLY ORGANISED?

3.1 | Number, size and spatial arrangement

Figure 2 shows a scene with a mean cell size $\overline{S}$ of about 9 km and cell sizes ranging between 2.8 and 20.7 km. Therewith, the scene is exemplary for a large mean rain cell size during EUREC^{4}A (Fig. 3a) and represents well the range of observed cell sizes (Fig. 5a). Figure 5a shows that a cell size larger than 20 km was rarely observed. The slope of the distribution of cell sizes falls towards high cell sizes. This was similarly noted by Trivej and Stevens (2010) for precipitation cells in the RICO campaign. About 50 % of the cells have a size of less than 5 km, 10 % of the cells have a size of more than 10 km. We investigate how the mean cell size relates to the individual cell sizes in a scene. Fig. 5b

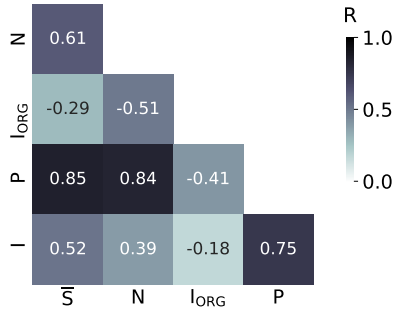

FIGURE 4 Spearman correlation coefficient R between cell number N, mean cell size $\overline{S}$, the cells' spatial arrangement quantified by the I_{ORG}, precipitation amount P and precipitation intensity I, coloured according to the absolute correlation between a variable pair.

shows that the maximum cell size and spread in cells sizes increase with the mean cell size. Both are strongly correlated with the mean cell size with correlation coefficients of 0.89 and 0.83, respectively. This suggests that it is not a similar growth of all cells but that of a few, that drives the growth of mean cell size. Processes that trigger this growth for a few cells thus probably have a dominant role, e.g the merging of cells or colliding cold pools that trigger large rain cells.

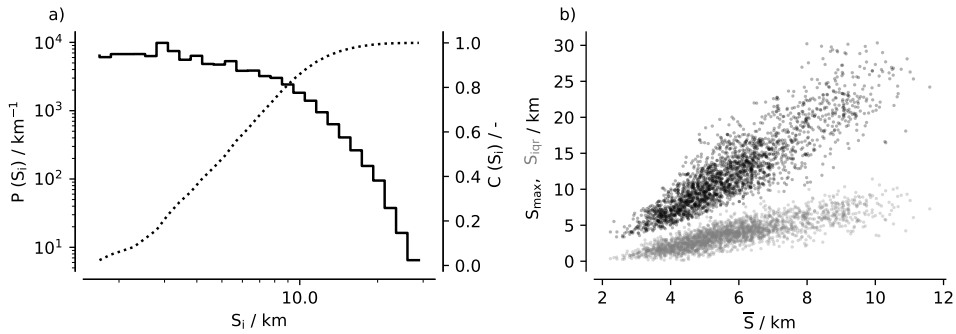

FIGURE 5 a) Distribution of cell sizes $P(S_i)$ (solid line) and cumulative distribution of cell sizes $C(S_i)$ (dashed line). b) Maximum cell size S_{max} (dark color) and cell size spread, quantified as the interquartile range of cell sizes S_{iqr} (light color), as a function of mean cell size $\overline{S}$ per scene.

The joint frequency of occurrence of mean cell size $\overline{S}$ and cell number N is shown in Fig. 6. The example scene contains 24 cells, which is exemplary for a moderate rain cell number N during EUREC^{4}A. About 60 % of scenes contained less than 20 cells and most frequently, scenes contained a small cell number between 5 and 15, and a mean cell size of around 5 km. Fig. 6 shows that N and $\overline{S}$ are positively correlated as quantified by the correlation coefficient of 0.61 (Fig. 4). This is observed differently in radar scans measuring the number and size of rain cells in deep tropical convection (Darwin radar observations; Louf et al., 2019). These observations show, if anything, a negative correlation

between cell number and size. The difference between Darwin and EUREC^{4}A possibly reflects a difference between shallow and deep convection. As the rain fraction in the trades is lower, the largest rain cells do not prevent a high cell number to occur in the same scene. Given their positive correlation, the phase space of $\overline{S}$ and N spanned here, which we will use in our subsequent analysis, allows us to examine the relationship of a variable with cell number separately from the relationship of the same variable with cell size.

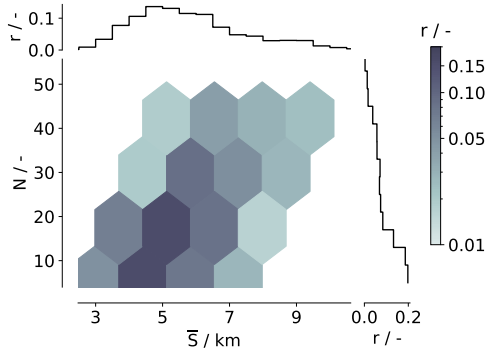

FIGURE 6 Joint relative frequency of occurrence of mean cell size $\overline{S}$ and number of cells N with individual histograms.

In the example scene, the cells are distributed at an average distance of 70 km (L_A) or 15 km if only the distance to the nearest neighbour is taken into account (L_{NN}). Fig. 7a-b shows how these two properties, L_A and L_{NN}, varied during EUREC^{4}A and that L_A and L_{NN} in the example scene are typical observed distances. Most frequently a L_A around 65 km and L_{NN} around 14 km were observed. The distribution of L_{NN} is unimodal and skewed towards higher L_{NN} (Fig. 7b). L_{NN} varies only in a narrow range, that is, rain cells have a typical distance to their neighbouring cell. The distribution of L_A shows a less marked peak and is skewed towards small L_A (Fig. 7a). Possibly, cold pools (e.g. visible in Fig. 2 with the typical arc-shaped pattern) smooth and widen the distribution of L_A by their varying strength and extent.

If the rain cells in the example scene were randomly distributed, L_A would be around 90 km and L_{NN} around 19.5 km. That is, the observed distances are shorter than the random distances and this scene shows a clustered state, which is classified by an I_{ORG} of 0.67 (Fig. 2). As indicated in Fig. 7a-b and shown in Fig. 7c, the rain cells arrangement is clustered in almost all scenes (I_{ORG} > 0.5). This was similarly found in studies of deep convection (e.g. Brueck et al., 2020; Pscheidt et al., 2019). That the spatial arrangement in scenes of precipitation is typically clustered fits with the idea that precipitation processes develop in cloud complexes or clusters and that these represent inhomogeneities. Precipitation does not occur randomly but due to inhomogeneities in a field and therewith clustered.

We now analyse how the cells' spatial arrangement, cell number and size covary by analysing the I_{ORG} in the $\overline{S}$-N phase space spanned before (Fig. 8a). The analysis reveals three main findings. First, few cells (small N) are more clustered (higher I_{ORG}) than many cells (high N). For a given $\overline{S}$, I_{ORG} decreases with N. That is, clustering and cell number are negatively correlated (R = -0.51, Fig. 4). Brueck et al. (2020), noting the same relationship, point to thermodynamical considerations that can help explain this behaviour. When conducting idealized simulations, it can be seen that in

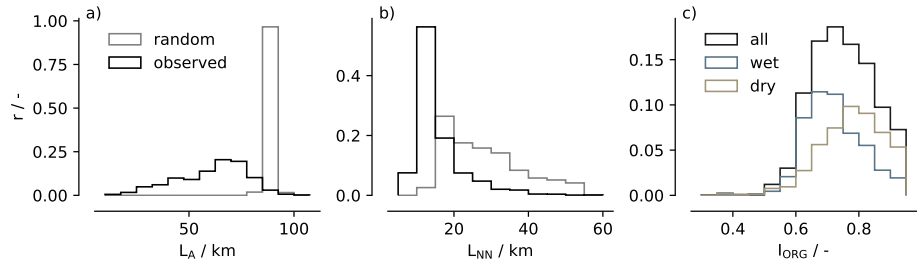

FIGURE 7 Relative frequency of a) mean distance between all possible pairs of cells L_A, b) mean distance between nearest-neighbour cells L_{NN} and c) the I_{ORG} for all, dry ($W >$ median (W)) and wet scenes ($W <$ median (W)).

a scene starting from homogeneous thermodynamical conditions, many randomly distributed cells appear, whereas in the presence of inhomogeneities, the number of cells in a scene can be limited. By subsampling the scenes into four composites representing the four corners of the $\overline{S}$-N phase space (Fig. 9) to show the variability in each composite, we further note that scenes with few cells have a wider range of possible spatial arrangements than scenes with many cells (Fig. 9c). Especially few and small cells, indicative of little precipitation, occur in a variety of spatial arrangements, which fits the subjective analysis of radar and satellite imagery during the RICO campaign (Rauber et al., 2007).

Second, variations of clustering with cell size are more complex than with cell number. While I_{ORG} increases with $\overline{S}$ in scenes with a small N, in scenes with a large N, I_{ORG} decreases with $\overline{S}$ (Fig. 8a). Thus, overall, the correlation between $\overline{S}$ and I_{ORG} is weak (R = -0.29, Fig. 4). Third, the I_{ORG} hence maximizes in the lower right corner of the $\overline{S}$-N phase space (Fig. 8a), that is, clustering is typically highest where cells are few and on average large (see also Fig. 9c). This was similarly found in storm resolving simulations of deep tropical convection (Brueck et al., 2020), except that here the degree of clustering increases with mean cell size at all cell numbers. The difference between shallow and deep convection might be explained by the idea that deep convective precipitation often originates from large precipitating systems, where large cells are part of a large convective object and hence clustered, whereas trade wind showers can also be associated with less organised precipitation systems, as suggested by the gravel cloud pattern (Stevens et al., 2020). Nevertheless, our analysis suggests that the organisation of precipitation in trade wind shallow convection shares similarities to deep convection in that clustering and cell number are negatively correlated and the degree of clustering is typically highest in scenes containing few and, on average, large cells. Next, we will show how the different scaling of I_{ORG} with $\overline{S}$ in regimes of small and large N is related to different moisture regimes.

3.2 | Moisture environment

Past studies have shown that water vapour path is related to precipitation (e.g. Bretherton et al., 2004; Nuijens et al., 2009) as well as organisation (e.g. Bretherton et al., 2005; Tobin et al., 2012). Investigating W in the $\overline{S}$-N phase space (Fig. 8b), we identify two regimes: a moist regime (high W) at high cell number and a dry regime (low W) at low cell number. Differences in the water vapour path mainly appear in the number of rain cells and only slightly in the mean size of the cells. While W increases with N for a given $\overline{S}$, for a given N, the correlation of W with $\overline{S}$ is not obvious. For a large N, W tends to increase with $\overline{S}$, but for a small N, W varies weakly with $\overline{S}$. Hence, dry and moist scenes differ predominantly through the number of cells, whereas the mean area of the cells only varies weakly with W. This was also found in radar observations (Louf et al., 2019) and simulations (Brueck et al., 2020) of deep convection. In

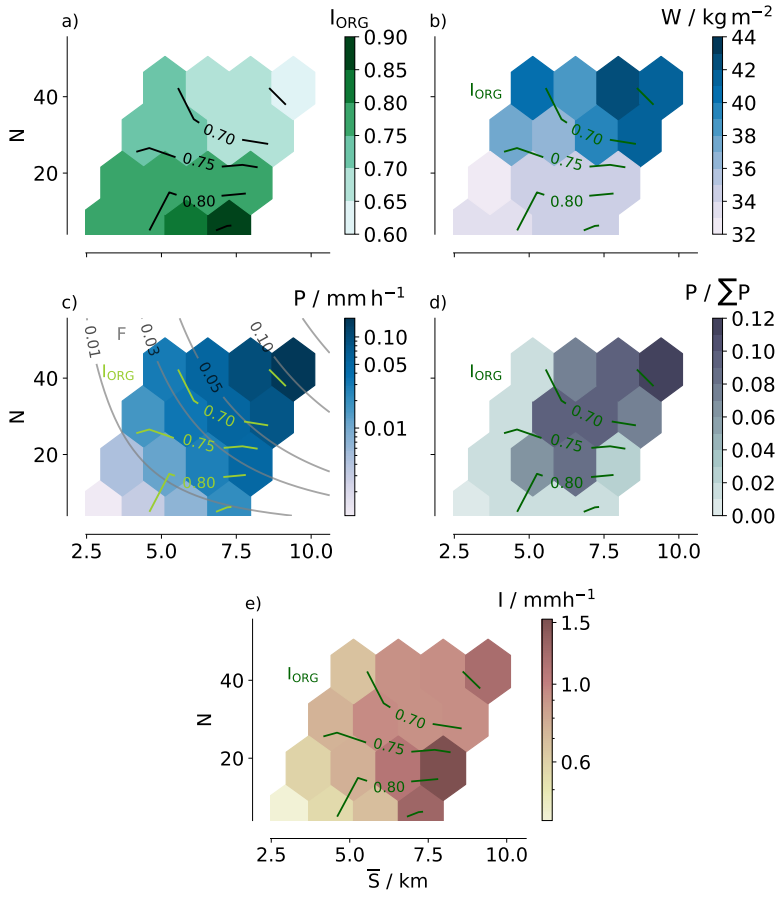

FIGURE 8 a) I_{ORG}, b) integrated water vapour W, c) precipitation amount P, d) contribution to total precipitation $P/\sum P$, e) precipitation intensity I as a function of mean cell size $\overline{S}$ and cell number N.

a moist environment, clouds may be less affected by entrainment, which allows them to reach deeper and eventually start to precipitate (Smalley and Rapp, 2020). Also, clouds and hence precipitating cells may live longer in moister environments. Both could explain the enhanced cell numbers in moist compared to dry environments.

A comparison of W and the I_{ORG} in the $\overline{S}$-N phase space (Fig. 8b) shows that scenes with a small N are typically dryer and show a higher degree of clustering than scenes with a large N (see also Fig. 9d). Fig. 7c displays the histogram of I_{ORG} in moist versus dry scenes. In dry scenes, the distribution shifts towards a higher degree of clustering. This agrees with idealized studies of radiative convective equilibrium (Bretherton et al., 2005; Muller and Held, 2012) and observations (e.g. Tobin et al., 2012), which show that aggregated or clustered states of deep convection are typically drier. Possibly, isolated rain cells, that is with a low degree of clustering, can hardly exist in dry environments as they are strongly affected by entrainment. Clustering might reduce the updraft buoyancy reduction through entrainment, allowing cells to develop in hostile, dry environments (Becker et al., 2018).

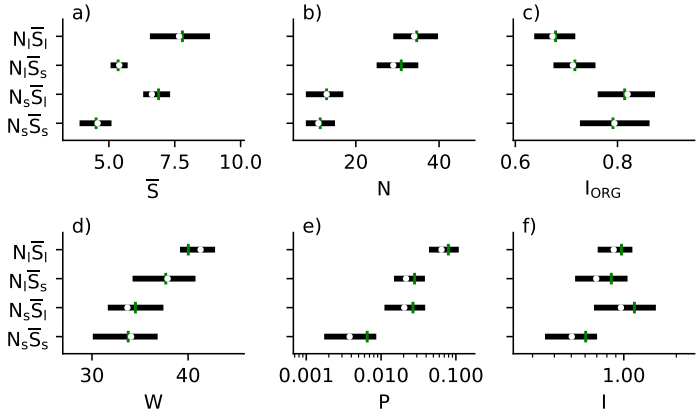

FIGURE 9 Interquartile range (black box), median (white dot) and mean (green line) of mean cell size $\overline{S}$, cell number N, and I_{ORG} for four composites representing the four corners in the $\overline{S}$-N phase space with $N_s < 20$, $N_l > 20$, $\overline{S}_s < 6$ km, $\overline{S}_l > 6$ km. The number of scenes is equal in each composite.

4 | HOW DOES SPATIAL ORGANISATION MATTER FOR PRECIPITATION CHARACTERISTICS?

4.1 | Precipitation amount

First, we analyse how precipitation amount varies as a function of cell size and number. Figure 8c shows that for a given $\overline{S}$, P increases with N, and vice versa, for a given N, P increases with $\overline{S}$. Taken together, contours of P follow well the contour lines of rain fraction F. For the amount of precipitation, the intensity of rain showers is hence of secondary importance, which is in agreement with previous studies, e.g. Nuijens et al. (2009). Because precipitation amount scales very well with precipitating fraction, P is strongly correlated with $\overline{S}$ and N ($R \approx 0.85$, Fig. 4). Consequently, precipitation amounts can be similar for scenes with few and on average large cells or many and on average small cells that have a similar rain fraction, and scenes with numerous and on average large cells exhibit on average the highest precipitation amount (Fig. 9e).

We note two implications from the relationship of P with N and $\overline{S}$. First, although scenes with a mean cell size of ~ 5 km and small cell number occur most frequently, they do not contribute the most to the total precipitation during EUREC^{4}A (Fig. 8d). Figure 8d shows that the precipitation contribution is shifted to larger and more numerous cells compared to the frequency distribution (Fig. 6). Although they occur rarely, scenes with the largest and most numerous cells do contribute the most to the total precipitation, because of their high rain rate. Additionally, a moderate cell size and number contribute substantially to the total precipitation through a combination of a moderate rain rate and moderate frequency of occurrence.

Second, as $\overline{S}$ is strongly correlated to the maximum rain cell size and cell size spread (see Sect. 3), with an increase in P, the cell size spread and maximum cell size increases. This fits observations by Trivej and Stevens (2010) from the RICO campaign, who highlight that especially large cells at the tail of the size distribution vary with precipitation area, which we confirm determines to a first order the precipitation amount. We find that on average the 20 % largest cells

in a scene have a mean cell size 2.5 times larger than the mean scene cell size, contribute half to the precipitating area and 60 % to the precipitation amount. This contribution increases up to 70 % in the 10 % rainiest scenes (not shown). That is, as the amount of precipitation in a scene increases, the precipitation is distributed more unevenly across the cells.

Recalling our previous analyses, P varies differently as a function of $\overline{S}$ and N than the I_{ORG}. Comparing P and the I_{ORG} in the $\overline{S}$-N phase space (Fig. 8c) shows that P increases with $\overline{S}$ and N, whereas the I_{ORG} decreases with N and varies differently as a function of $\overline{S}$ for small and large N. At large N, I_{ORG} decreases with $\overline{S}$. In the upper part of the $\overline{S}$-N phase space, contours of P and I_{ORG} tend thus to be roughly parallel. While precipitation amount maximizes in the upper right corner of the $\overline{S}$-N phase space, at large N and $\overline{S}$, the degree of clustering minimizes here, suggesting both are negatively correlated with each other (see also Fig. 9c, e). At small N, however, I_{ORG} increases with $\overline{S}$, so that in the lower part of the $\overline{S}$-N phase space, contours of P and I_{ORG} are perpendicular to each other, i.e. suggesting they vary independently and that the same precipitation amounts occur in scenes with a varying degree of clustering. Scenes with small N and large $\overline{S}$ that show on average the highest degree of clustering, exhibit moderate precipitation amounts likewise as scenes with more numerous but smaller cells that show a lower degree of clustering (Fig. 9c, e). Across the whole datasets, the relationship between precipitation amount and clustering is therefore negative but foremost weak (R = -0.41, Fig. 4).

These analyses hence suggest that hypothesized mechanisms, such as that clustering increases precipitation through cell interaction, play overall no or a subordinate role for the precipitation amount in a scene because precipitation amount increases with the rain fraction maximizing where cells are large and numerous while the degree of clustering maximizes where cells are large but few. We find that scenes with small N and large $\overline{S}$, that show on average a high degree of clustering, also contribute little to the total observed precipitation amount (Fig. 8d). This suggests that scenes with a high degree of clustering neither precipitate the most nor occur frequently enough to contribute much to the precipitation amount and, hence, that the spatial arrangement of rain cells is of second order importance for precipitation amount in the trades. Similar conclusions were drawn for deep convection (e.g Brueck et al., 2020; Pscheidt et al., 2019).

Only when considering the moisture environment, a positive effect of clustering on precipitation amounts may be seen. Combining the results of Fig 8b and c, at small N, in the dry regime, precipitation amount is higher for scenes with larger $\overline{S}$ that show a higher degree of clustering. Further, keeping precipitation amount constant while moving in the $\overline{S}$-N phase space into scenes with small N, which are dry, the mean cell size increases as compensation and with it, the degree of clustering. In this sense, clustering may be considered important for maintaining precipitation amounts in dry environments as similarly found by Brueck et al. (2020) for deep convection.

4.2 | Precipitation Intensity

First, we analyse the relationship between precipitation intensity, cell number and mean cell size using the $\overline{S}$-N phase space. Figure 8e shows that for a given N, I increases with $\overline{S}$. For a given $\overline{S}$, I does not systematically increase or decrease with N. Consequently, the positive correlation between I and N across the whole dataset (R = 0.39, Fig. 4) is due to an increase of I with $\overline{S}$ (R = 0.52, Fig. 4) and the covariation of N with S (R = 0.61, Fig. 4). While both cell number and size are important for the precipitation amount in the trades, it seems predominantly the latter for precipitation intensity. This was similarly found in radar observations of deep tropical convection (Louf et al., 2019) and is

e.g. important for cumulus parametrizations, where the convective area is a key ingredient. Whereas the convective or precipitating area well describes the precipitation amount, its composition into cell size and number is decisive for precipitation intensity.

Possible explanations for why precipitation intensity increases with mean cell size are that large cells protect their updrafts better from dilution by entrainment and stronger updrafts enhance the precipitation intensity (e.g. Kirshbaum and Grant, 2012). Also, large cells may dissipate more slowly, i.e. they live longer, and therefore develop a moister (sub)cloud layer that leads to less evaporation of the falling raindrops. Here, we can only quantify this effect. To do so, we investigate how the rain intensity of an individual cell scales with its size, shown in Fig. 10 for the mean and maximum rain intensity of a cell. Both, maximum and mean rain intensity, increase with cell size for cell sizes above 3 km. Cells with a size around 10 km have a mean intensity around 1 mm h^{-1}. A maximum intensity above 1 mm h^{-1} occurs in cells larger than roughly 5 km. As roughly 50 % of cells are larger than 5 km (see §3.1), roughly 50 % of the cells exhibit maximum intensities above 1 mm h^{-1}, a threshold associated with the formation of cold pools in past studies (e.g. Barnes and Garstang, 1982; Drager and van den Heever, 2017).

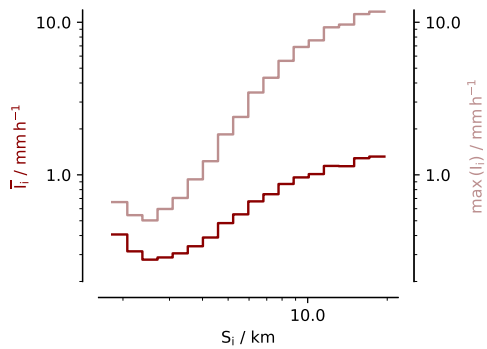

FIGURE 10 Mean Intensity $\overline{I_i}$ and maximum intensity max(I_i) of a cell binned as a function of cell size.

The analysis of I in the $\overline{S}$-N phase space further shows that the increase of I with $\overline{S}$ differs between small and large N (Fig. 8e). In scenes with small N, the increase of I with $\overline{S}$ is stronger than in scenes with large N. Our previous analyses identified a moist regime at large N and a dry regime at small N (§3.2), suggesting that I increases more strongly with $\overline{S}$ in dry compared to moist scenes and that precipitation intensities are thus highest in dry scenes. Figure 11a,b confirms this. The distribution of precipitation intensities in dry scenes shows a higher variability and extends to larger values than in moist scenes. That precipitation intensity is highest at rather low water vapour paths contradicts the hypotheses, e.g. put forward by (Nuijens et al., 2009), that precipitation intensity increases with cloud depth, and cloud depth increases with the water vapour path. For deep convection, Louf et al. (2019), however, similarly observed that precipitation intensity is highest at dry environments. Because I increases with $\overline{S}$, I increases with precipitation fraction F (Fig. 11c). This increase is again stronger for dry than for moist scenes. Thus, for the same rain fraction in a dry compared to a moist environment, moving from one case with small $\overline{S}$ but large N to one case with large $\overline{S}$ and small N, precipitation amount increases.

Our previous analyses show that dry and moist scenes typically also exhibit differences in the degree of clustering.

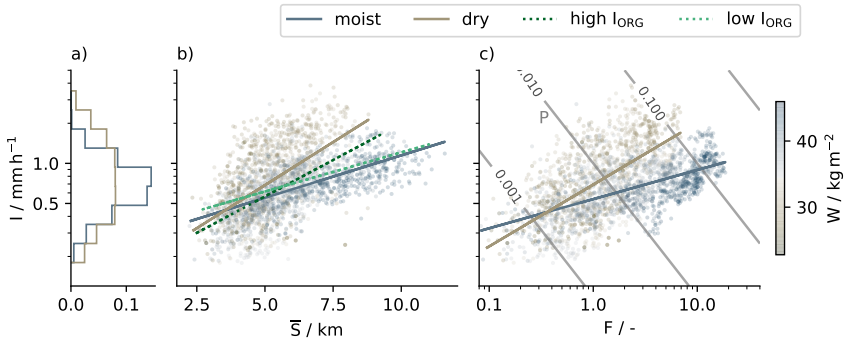

FIGURE 11 a) Relative frequency of precipitation intensity I for dry (W > median (W)) and wet scenes (W < median (W)). I as a function of b) mean cell size $\overline{S}$ and c) rain fraction F. The shading in b) and c) denotes the water vapour path W. The lines in b) and c) denotes the fit for dry and wet scenes or scenes with high I_{ORG} (I_{ORG} > p75 (I_{ORG})) and low I_{ORG} (I_{ORG} < p25 (I_{ORG})).

Figure 11 shows that the increase of I with $\overline{S}$ is stronger in scenes with a high degree of clustering than in scenes with a low degree of clustering. Possibly, clustering plays a role in the different scaling of precipitation intensity with cell size in dry and moist environments. We compare the variations of precipitation intensity and clustering in the $\overline{S}$-N phase space (Fig. 8e). At large N or moist environments, I increases with $\overline{S}$, whereas I_{ORG} decreases with $\overline{S}$. At small N or in dry environments, both I and I_{ORG} increase with $\overline{S}$. Thus both I and I_{ORG} maximize where $\overline{S}$ is large and N is small (see also Fig. 9c,f). The analyses hence suggest that clustering is important for precipitation in dry environments. For a given mean cell size of about 7 km, I and the degree of clustering increase as one moves from scenes with large N in the moist regime to scenes with a small N in the dry regime (Fig. 8e). Overall, however, I and I_{ORG} vary mostly perpendicular to each other in the $\overline{S}$-N phase space (Fig. 8e), so that across all regimes the correlation between clustering and precipitation intensity is weak (R = -0.18, Fig. 4).

5 | DIURNAL CYCLE

Our analysis so far takes a snapshot view of precipitation. To probe the evolution of the rain cells' spatial organisation, we lastly look at the diurnal cycle, a prominent mode of variability in the tropics, revisited recently by Vial et al. (2019). Measurements from the RICO field experiment show a nighttime to early morning peak and an afternoon minimum in precipitation in trade wind convection (Nuijens et al., 2009; Snodgrass et al., 2009), confirmed by the analyses of Vial et al. (2019). Fig. 12 shows this daily cycle captured in our dataset. Please note that the diurnal cycle is not complete on all days due to gaps in the measurements.

Precipitation amount peaks in the early morning and has its minimum in the late afternoon before sunset (Fig. 12a). The diurnal cycle of N and $\overline{S}$ roughly follow P (Fig. 12c,d), which matches our previous analyses (§4). However, N tends to peaks before $\overline{S}$. At the same time, rain cells exhibit a low degree of clustering (Fig. 12e). $\overline{S}$ stays high as N already decreases. This indicates that small cells might dissipate earlier whereas large cells live longer and/or that merging of cells is enhanced. Cells are now spaced closed to each other indicated by a large I_{ORG}. These variations fit the variations of the cloud patterns Gravel, Flowers and Fish (Vial et al., 2021). Gravel, characterized by small,

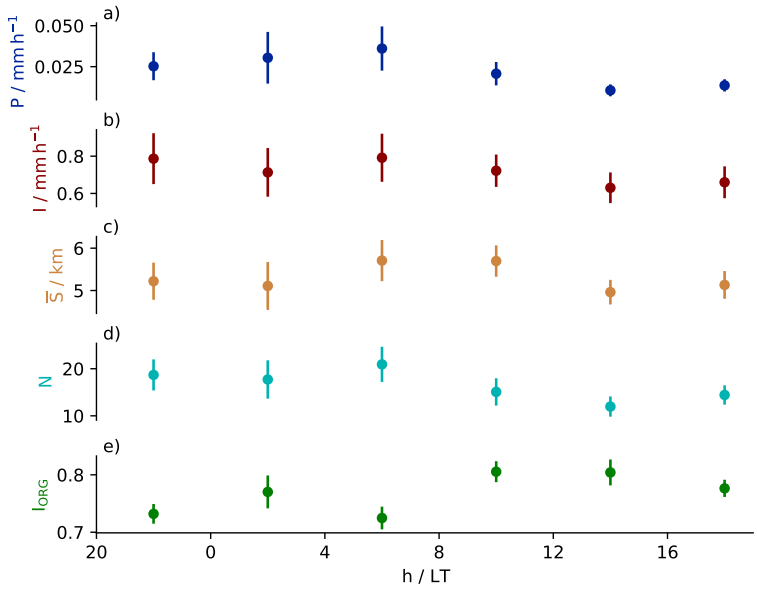

FIGURE 12 Mean diurnal cycle of a) precipitation amount P, b) precipitation intensity I, c) cell number N, d) mean cell size $\overline{S}$, and e) the cells' spatial arrangement quantified by the I_{ORG}. Error bars denote the uncertainty in the mean (standard error).

numerous, and scattered cells, has a peak occurrence around midnight. Flowers, characterized by larger cells, have a peak occurrence before sunrise and fish, characterized by larger and more clustered cells, has a peak occurrence around noon. The daytime, where $\overline{S}$ slowly decreases and I_{ORG} is high, is also characterized by a relatively high precipitation intensity (Fig. 12b). Precipitation intensity does not show a clear diurnal cycle. Vogel et al. (2021) find that cold pools extend the diurnal cycle of precipitation into the early afternoon, possibly shaping this behaviour seen here. Figure 12 shows that the relationships revealed by our previous analyses, are evident on the diurnal time scale and indicates that the number, size, and spatial arrangement of rain cells might also be related to the cells' life cycle.

6 | SUMMARY AND CONCLUSION

This study investigates the spatial behaviour of precipitating trade wind convection and how it matters for precipitation characteristics in the trades as observed during the EUREC^{4}A field campaign. To do so, scenes of trade wind convection scanned by the C-band radar Poldirad are examined. We investigate the spatial organization in these scenes by analysing the size, number and spatial arrangement of rain cells and how these relate to the scene's precipitation amount and intensity. Further, we include water vapour path as explanatory variable.

During EUREC^{4}A, a mean rain cell size of 5 km and a mean distance to the nearest neighbour of about 14 km were most common. Up to 60 cells in one scene and a mean cell size of 12 km were observed. In nearly all scenes, cells were spaced closer than in a random distribution. That is, the spatial arrangement in scenes of precipitation is almost always clustered, which is in line with the expectation that precipitation is related to inhomogeneities. In the diurnal cycle, cell number tends to peak before mean cell size in the early morning, and the degree of clustering, which peaks

around noon. This is in line with the diurnal cycle of cloud patterns (Vial et al., 2021) and the relationships between cell number, size and arrangement that our analyses show. While cell number and mean size are positively correlated and cell number and clustering are negatively correlated, the relationship between mean cell size and clustering is less obvious and differs between scenes with a high and low cell number. Scenes with a few and on average large cells exhibit typically the highest degree of clustering, which was similarly found for deep convection (Brueck et al., 2020; Senf et al., 2019). This suggests similarities between the spatial organisation of shallow and deep precipitating convection.

We identify two regimes: a moist regime at high cell number and a dry regime at low cell number. In the dry regime the degree of clustering is typically higher than in the moist regime. Clustering might reduce the updraft buoyancy reduction through entrainment, allowing cells to develop in hostile, dry environments (Becker et al., 2018). While we find a systematic relationship between water vapor path, cell number and the degree of clustering, the relationship between water vapour path and cell size is less clear. Regarding the close relationship between water vapour availability and precipitation in the trades highlighted in Nuijens et al. (2009), our analyses suggest that precipitation increases with water vapour path predominantly because of more numerous cells that are more scattered rather than larger cells. We conclude that the relationship between water vapour path and precipiation is reflected in two specific attributes of spatial organisation - the cell number and arrangement -, whereas cell size seems of secondary importance for the relationship between water vapour path and precipitation.

We conclude that the amount and intensity of precipitation are influenced differently by the spatial organisation in trade wind precipitation fields:

- The amount of precipitation varies closely with cell number and mean cell size because it scales well with rain fraction. Highest precipitation amounts typically occur in scenes that contain numerous and on average large cells and show a low degree of clustering.
- The intensity of precipitation increases predominantly with mean cell size. This increase, however, differs with the moisture regime. It is stronger in dry scenes at low cell number than in moist scenes at high cell number. Highest precipitation intensities hence typically occur in dry scenes that contain on average large and few cells and show a high degree of clustering.

Our analyses suggest that clustering is important for precipitation formation in dry environments. Clustering might act by protecting cells from their hostile dry environment allowing cells and also larger cells to develop. Across all regimes, precipitation characteristics and clustering are, however, negatively and predominantly weakly correlated and hence the spatial arrangement of cells is of second order importance for precipitation in the trades. This was similarly found for deep convection (e.g. Brueck et al., 2020; Pscheidt et al., 2019). From the three spatial attributes investigated, cell size and number are equally strongly related to precipitation amount, and cell size is best related to precipitation intensity. Our analyses thus highlight the importance of cell size and raise the question of whether processes within cells, such as updraft strength, or between cells, such as moistening or merging and generation of subsequent cells, matter for the size of rain cells. We show that understanding how trade wind convection organises into different rain cell sizes matters for both the amount and intensity of precipitation, and hence for the heating and drying rates and triggering of cold pools in the trades.

Acknowledgements

This research was funded by the Deutsche Forschungsgemeinschaft (DFG, German Research Foundation) under Germany's Excellence Strategy – EXC 2037 'CLICCS - Climate, Climatic Change, and Society' – Project Number: 390683824, contribution to the Center for Earth System Research and Sustainability (CEN) of Universität Hamburg. We would like to thank Raphaela Vogel for valuable comments on the draft. The authors declare no conflict of interest. The data used in this publication was gathered in the EUREC^{4}A field campaign and is published by Hagen et al. (2021) and Bock et al. (2021) and available on the EUREC^{4}A AERIS database via https://doi.org/10.25326/217 and https://doi.org/10.25326/79. EUREC^{4}A is funded with support of the European Research Council (ERC), the Max Planck Society (MPG), the German Research Foundation (DFG), the German Meteorological Weather Service (DWD) and the German Aerospace Center (DLR).

references

Barnes, G. M. and Garstang, M. (1982) Subcloud Layer Energetics of Precipitating Convection. *Monthly Weather Review*, **110**, 102–117.

Becker, T., Bretherton, C. S., Hohenegger, C. and Stevens, B. (2018) Estimating Bulk Entrainment With Unaggregated and Aggregated Convection. *Geophysical Research Letters*, **45**, 455–462.

Betts, A. K. (1997) Trade Cumulus: Observations and Modelling. In *The Physics and Parameterization of Moist Atmospheric Convection* (ed. R. K. Smith), 99–126. Dordrecht: Springer Netherlands.

Bock, O., Bosser, P., Flamant, C., Doerflinger, E., Jansen, F., Fages, R., Bony, S. and Schnitt, S. (2021) IWV observations in the Caribbean Arc from a network of ground-based GNSS receivers during EUREC 4 A. *Earth System Science Data*, 1–51.

Bony, S. and Dufresne, J.-L. (2005) Marine boundary layer clouds at the heart of tropical cloud feedback uncertainties in climate models. *Geophysical Research Letters*, **32**.

Bony, S., Schulz, H., Vial, J. and Stevens, B. (2020) Sugar, Gravel, Fish, and Flowers: Dependence of Mesoscale Patterns of Trade-Wind Clouds on Environmental Conditions. *Geophysical Research Letters*, **47**.

Bony, S., Stevens, B., Ament, F., Bigorre, S., Chazette, P., Crewell, S., Delanoë, J., Emanuel, K., Farrell, D., Flamant, C., Gross, S., Hirsch, L., Karstensen, J., Mayer, B., Nuijens, L., Ruppert, J. H., Sandu, I., Siebesma, P., Speich, S., Szczap, F., Totems, J., Vogel, R., Wendisch, M. and Wirth, M. (2017) EUREC4A: A Field Campaign to Elucidate the Couplings Between Clouds, Convection and Circulation. *Surveys in Geophysics*, **38**, 1529–1568.

Bretherton, C. S. and Blossey, P. N. (2017) Understanding Mesoscale Aggregation of Shallow Cumulus Convection Using Large-Eddy Simulation. *Journal of Advances in Modeling Earth Systems*, **9**, 2798–2821.

Bretherton, C. S., Blossey, P. N. and Khairoutdinov, M. (2005) An Energy-Balance Analysis of Deep Convective Self-Aggregation above Uniform SST. *Journal of the Atmospheric Sciences*, **62**, 4273–4292.

Bretherton, C. S., Peters, M. E. and Back, L. E. (2004) Relationships between Water Vapor Path and Precipitation over the Tropical Oceans. *Journal of Climate*, **17**, 1517–1528.

Brueck, M., Hohenegger, C. and Stevens, B. (2020) Mesoscale marine tropical precipitation varies independently from the spatial arrangement of its convective cells. *Quarterly Journal of the Royal Meteorological Society*, **146**, 1391–1402.

Denby, L. (2020) Discovering the Importance of Mesoscale Cloud Organization Through Unsupervised Classification. *Geophysical Research Letters*, **47**, 1–10.

Drager, A. J. and van den Heever, S. C. (2017) Characterizing convective cold pools. *Journal of Advances in Modeling Earth Systems*, **9**, 1091–1115.

Hagen, M., Ewald, F., Groß, S., Oswald, L., Farrell, D., Forde, M., Gutleben, M., Heumos, J., Reimann, J., Tetoni, E., Marinou, E., Möller, G., Kiemle, C., Li, Q., Chewitt-Lucas, R., Daley, A., Grand, D. and Hall, K. (2021) Deployment of the C-band radar Poldirad on Barbados during EUREC4A. *Earth Syst. Sci. Data [preprint; essd-2021-203]*, 1–26.

Kirshbaum, D. J. and Grant, A. L. M. (2012) Invigoration of cumulus cloud fields by mesoscale ascent. *Quarterly Journal of the Royal Meteorological Society*, **138**, 2136–2150.

Lau, K. M. and Wu, H. T. (2003) Warm rain processes over tropical oceans and climate implications. *Geophysical Research Letters*, **30**, 2–6.

Louf, V., Jakob, C., Protat, A., Bergemann, M. and Narsey, S. (2019) The Relationship of Cloud Number and Size With Their Large-Scale Environment in Deep Tropical Convection. *Geophysical Research Letters*, **46**, 9203–9212.

Marshall, J. S., Hitschfeld, W. and Gunn, K. L. S. (1955) Advances in Radar Weather. In *Advances in Geophysics* (ed. H. E. Landsberg), vol. 2, 1–56. Elsevier.

Muller, C. J. and Held, I. M. (2012) Detailed Investigation of the Self-Aggregation of Convection in Cloud-Resolving Simulations. *Journal of the Atmospheric Sciences*, **69**, 2551–2565.

Nuijens, L., Emanuel, K., Masunaga, H. and L'Ecuyer, T. (2017) Implications of Warm Rain in Shallow Cumulus and Congestus Clouds for Large-Scale Circulations. *Surveys in Geophysics*, **38**, 1257–1282.

Nuijens, L., Stevens, B. and Siebesma, A. P. (2009) The environment of precipitating shallow cumulus convection. *Journal of the Atmospheric Sciences*, **66**, 1962–1979.

Pscheidt, I., Senf, F., Heinze, R., Deneke, H., Trömel, S. and Hohenegger, C. (2019) How organized is deep convection over Germany? *Quarterly Journal of the Royal Meteorological Society*, **145**, 2366–2384.

Rasp, S., Schulz, H., Bony, S. and Stevens, B. (2019) Combining crowd-sourcing and deep learning to explore the meso-scale organization of shallow convection. *arXiv*, 1980–1995.

Rauber, R. M., Stevens, B., Ochs, H. T., Knight, C., a. Albrecht, B., Blyth, a. M., Fairall, C. W. and Jensen, J. B. (2007) Over the ocean: The RICO campaign. *Bulletin of the American Meteorological Society*, 1912–1928.

Retsch, M. H., Jakob, C. and Singh, M. S. (2020) Assessing Convective Organization in Tropical Radar Observations. *Journal of Geophysical Research: Atmospheres*, **125**.

Schroth, A. C., Chandra, M. S. and Meischner, P. F. (1988) A C -Band Coherent Polarimetric Radar for Propagation and Cloud Physics Research. *Journal of Atmospheric and Oceanic Technology*, **5**, 803–822.

Schulz, H., Eastman, R. and Stevens, B. (2021) Characterization and Evolution of Organized Shallow Convection in the Downstream North Atlantic Trades. *Journal of Geophysical Research: Atmospheres*, **126**, e2021JD034575.

Seifert, A. and Heus, T. (2013) Large-eddy simulation of organized precipitating trade wind cumulus clouds. *Atmospheric Chemistry and Physics*, **13**, 5631–5645.

Senf, F., Brueck, M. and Klocke, D. (2019) Pair correlations and spatial statistics of deep convection over the Tropical Atlantic. *Journal of the Atmospheric Sciences*, **76**, 3211–3228.

Short, D. A. and Nakamura, K. (2000) TRMM radar observations of shallow precipitation over the tropical oceans. *Journal of Climate*, **13**, 4107–4124.

Siebesma, A. P. (1998) Shallow Cumulus Convection. In *Buoyant Convection in Geophysical Flows* (eds. E. J. Plate, E. E. Fedorovich, D. X. Viegas and J. C. Wyngaard), 441–486. Dordrecht: Springer Netherlands.

Smalley, K. M. and Rapp, A. D. (2020) The role of cloud size and environmental moisture in shallow cumulus precipitation. *Journal of Applied Meteorology and Climatology*, **59**, 535–550.

Snodgrass, E. R., Di Girolamo, L. and Rauber, R. M. (2009) Precipitation characteristics of trade wind clouds during RICO derived from Radar, Satellite, and aircraft measurements. *Journal of Applied Meteorology and Climatology*, **48**, 464–483.

Stevens, B. (2005) Atmospheric Moist Convection. *Annual Review of Earth and Planetary Sciences*, **33**, 605–643.

Stevens, B., Bony, S., Brogniez, H., Hentgen, L., Hohenegger, C., Kiemle, C., L'Ecuyer, T. S., Naumann, A. K., Schulz, H., Siebesma, P. A., Vial, J., Winker, D. M. and Zuidema, P. (2020) Sugar, gravel, fish and flowers: Mesoscale cloud patterns in the trade winds. *Quarterly Journal of the Royal Meteorological Society*, **146**, 141–152.

Stevens, B., Bony, S., Farrell, D., Ament, F., Blyth, A., Fairall, C., Karstensen, J., Quinn, P. K., Speich, S., Acquistapace, C., Aemisegger, F., Albright, A. L., Bellenger, H., Bodenschatz, E., Caesar, K.-A., Chewitt-Lucas, R., de Boer, G., Delanoë, J., Denby, L., Ewald, F., Fildier, B., Forde, M., George, G., Gross, S., Hagen, M., Hausold, A., Heywood, K. J., Hirsch, L., Jacob, M., Jansen, F., Kinne, S., Klocke, D., Kölling, T., Konow, H., Lothon, M., Mohr, W., Naumann, A. K., Nuijens, L., Olivier, L., Pincus, R., Pöhlker, M., Reverdin, G., Roberts, G., Schnitt, S., Schulz, H., Siebesma, A. P., Stephan, C. C., Sullivan, P., Touzé-Peiffer, L., Vial, J., Vogel, R., Zuidema, P., Alexander, N., Alves, L., Arixi, S., Asmath, H., Bagheri, G., Baier, K., Bailey, A., Baranowski, D., Baron, A., Barrau, S., Barrett, P. A., Batier, F., Behrendt, A., Bendinger, A., Beucher, F., Bigorre, S., Blades, E., Blossey, P., Bock, O., Böing, S., Bosser, P., Bourras, D., Bouruet-Aubertot, P., Bower, K., Branellec, P., Branger, H., Brennek, M., Brewer, A., Brilouet, P.-E., Brügmann, B., Buehler, S. A., Burke, E., Burton, R., Calmer, R., Canonici, J.-C., Carton, X., Cato Jr., G., Charles, J. A., Chazette, P., Chen, Y., Chilinski, M. T., Choularton, T., Chuang, P., Clarke, S., Coe, H., Cornet, C., Coutris, P., Couvreux, F., Crewell, S., Cronin, T., Cui, Z., Cuypers, Y., Daley, A., Damerell, G. M., Dauhut, T., Deneke, H., Desbios, J.-P., Dörner, S., Donner, S., Douet, V., Drushka, K., Dütsch, M., Ehrlich, A., Emanuel, K., Emmanouilidis, A., Etienne, J.-C., Etienne-Leblanc, S., Faure, G., Feingold, G., Ferrero, L., Fix, A., Flamant, C., Flatau, P. J., Foltz, G. R., Forster, L., Furtuna, I., Gadian, A., Galewsky, J., Gallagher, M., Gallimore, P., Gaston, C., Gentemann, C., Geyskens, N., Giez, A., Gollop, J., Gouirand, I., Gourbeyre, C., de Graaf, D., de Groot, G. E., Grosz, R., Güttler, J., Gutleben, M., Hall, K., Harris, G., Helfer, K. C., Henze, D., Herbert, C., Holanda, B., Ibanez-Landeta, A., Intrieri, J., Iyer, S., Julien, F., Kalesse, H., Kazil, J., Kellman, A., Kidane, A. T., Kirchner, U., Klingebiel, M., Körner, M., Kremper, L. A., Kretzschmar, J., Krüger, O., Kumala, W., Kurz, A., L'Hégaret, P., Labaste, M., Lachlan-Cope, T., Laing, A., Landschützer, P., Lang, T., Lange, D., Lange, I., Laplace, C., Lavik, G., Laxenaire, R., Le Bihan, C., Leandro, M., Lefevre, N., Lena, M., Lenschow, D., Li, Q., Lloyd, G., Los, S., Losi, N., Lovell, O., Luneau, C., Makuch, P., Malinowski, S., Manta, G., Marinou, E., Marsden, N., Masson, S., Maury, N., Mayer, B., Mayers-Als, M., Mazel, C., McGeary, W., McWilliams, J. C., Mech, M., Mehlmann, M., Meroni, A. N., Mieslinger, T., Minikin, A., Minnett, P., Möller, G., Morfa Avalos, Y., Muller, C., Musat, I., Napoli, A., Neuberger, A., Noisel, C., Noone, D., Nordsiek, F., Nowak, J. L., Oswald, L., Parker, D. J., Peck, C., Person, R., Philippi, M., Plueddemann, A., Pöhlker, C., Pörtge, V., Pöschl, U., Pologne, L., Posyniak, M., Prange, M., Quiñones Meléndez, E., Radtke, J., Ramage, K., Reimann, J., Renault, L., Reus, K., Reyes, A., Ribbe, J., Ringel, M., Ritschel, M., Rocha, C. B., Rochetin, N., Röttenbacher, J., Rollo, C., Royer, H., Sadoulet, P., Saffin, L., Sandiford, S., Sandu, I., Schäfer, M., Schemann, V., Schirmacher, I., Schlenczek, O., Schmidt, J., Schröder, M., Schwarzenboeck, A., Sealy, A., Senff, C. J., Serikov, I., Shohan, S., Siddle, E., Smirnov, A., Späth, F., Spooner, B., Stolla, M. K., Szkółka, W., de Szoeke, S. P., Tarot, S., Tetoni, E., Thompson, E., Thomson, J., Tomassini, L., Totems, J., Ubele, A. A., Villiger, L., von Arx, J., Wagner, T., Walther, A., Webber, B., Wendisch, M., Whitehall, S., Wiltshire, A., Wing, A. A., Wirth, M., Wiskandt, J., Wolf, K., Worbes, L., Wright, E., Wulfmeyer, V., Young, S., Zhang, C., Zhang, D., Ziemen, F., Zinner, T. and Zöger, M. (2021) EUREC^{4}A. *Earth System Science Data*, **13**, 4067–4119.

Stevens, B., Farrell, D., Hirsch, L., Jansen, F., Nuijens, L., Serikov, I., Brügmann, B., Forde, M., Linne, H., Lonitz, K. and Prospero, J. M. (2016) The Barbados cloud observatory: Anchoring investigations of clouds and circulation on the edge of the itcz. *Bulletin of the American Meteorological Society*, **97**, 735–754.

Tobin, I., Bony, S. and Roca, R. (2012) Observational evidence for relationships between the degree of aggregation of deep convection, water vapor, surface fluxes, and radiation. *Journal of Climate*, **25**, 6885–6904.

Tompkins, A. M. and Semie, A. G. (2017) Organization of tropical convection in low vertical wind shears: Role of updraft entrainment. *Journal of Advances in Modeling Earth Systems*, **9**, 1046–1068.

Touzé-Peiffer, L., Vogel, R. and Rochetin, N. (2021) Detecting cold pools from soundings during EUREC4A. *in review*.

Trivej, P. and Stevens, B. (2010) The echo size distribution of precipitating shallow cumuli. *Journal of the Atmospheric Sciences*, **67**, 788–804.

vanZanten, M. C., Stevens, B., Nuijens, L., Siebesma, A. P., Ackerman, A. S., Burnet, F., Cheng, A., Couvreux, F., Jiang, H., Khairoutdinov, M., Kogan, Y., Lewellen, D. C., Mechem, D., Nakamura, K., Noda, A., Shipway, B. J., Slawinska, J., Wang, S. and Wyszogrodzki, A. (2011) Controls on precipitation and cloudiness in simulations of trade-wind cumulus as observed during RICO. *Journal of Advances in Modeling Earth Systems*, **3**, n/a–n/a.

Vial, J., Dufresne, J. L. and Bony, S. (2013) On the interpretation of inter-model spread in CMIP5 climate sensitivity estimates. *Climate Dynamics*, **41**, 3339–3362.

Vial, J., Vogel, R., Bony, S., Stevens, B., Winker, D. M., Cai, X., Hohenegger, C., Naumann, A. K. and Brogniez, H. (2019) A New Look at the Daily Cycle of Trade Wind Cumuli. *Journal of Advances in Modeling Earth Systems*, 3148–3166.

Vial, J., Vogel, R. and Schulz, H. (2021) On the daily cycle of mesoscale cloud organization in the winter trades. *Quarterly Journal of the Royal Meteorological Society*, 2850–2873.

Villiger, L., Wernli, H., Boettcher, M., Hagen, M. and Aemisegger, F. (2021) Lagrangian formation pathways of moist anomalies in the trade-wind region during the dry season: Two case studies from EUREC^{4}A. *Weather and Climate Dynamics Discussions*, 1–49.

Vogel, R., Konow, H., Schulz, H. and Zuidema, P. (2021) A climatology of trade-wind cumulus cold pools and their link to mesoscale cloud organization. *Atmospheric Chemistry and Physics Discussions*, 1–32.

Vogel, R., Nuijens, L. and Stevens, B. (2016) The role of precipitation and spatial organization in the response of trade-wind clouds to warming. *Journal of Advances in Modeling Earth Systems*, **8**, 843–862.

Weger, R. C., Lee, J., Tianri Zhu and Welch, R. M. (1992) Clustering, randomness and regularity in cloud fields: 1. Theoretical considerations. *Journal of Geophysical Research*, **97**.

White, B. A., Buchanan, A. M., Birch, C. E., Stier, P. and Pearson, K. J. (2018) Quantifying the effects of horizontal grid length and parameterized convection on the degree of convective organization using a metric of the potential for convective interaction. *Journal of the Atmospheric Sciences*, **75**, 425–450.

Zuidema, P., Li, Z., Hill, R. J., Bariteau, L., Rilling, B., Fairall, C., Brewer, W. A., Albrecht, B. and Hare, J. (2012) On trade wind cumulus cold pools. *Journal of the Atmospheric Sciences*, **69**, 258–280.